SCIENTIFIC REP✸RTS

Porous Au-embedded WO$_3$ Nanowire Structure for Efficient Detection of CH$_4$ and H$_2$S

Nguyen Minh Vuong[1,2], Dojin Kim[1] & Hyojin Kim[1]

We developed a facile method to fabricate highly porous Au-embedded WO$_3$ nanowire structures for efficient sensing of CH$_4$ and H$_2$S gases. Highly porous single-wall carbon nanotubes were used as template to fabricate WO$_3$ nanowire structures with high porosity. Gold nanoparticles were decorated on the tungsten nanowires by dipping in HAuCl$_4$ solution, followed by oxidation. The surface morphology, structure, and electrical properties of the fabricated WO$_3$ and Au-embedded WO$_3$ nanowire structures were examined by scanning electron microscopy, transmission electron microscopy, X-ray diffraction, X-ray photoelectron spectroscopy, and current–voltage measurements. Formation of a nanowire structure resulted in significant enhancement in sensing response to H$_2$S and CH$_4$ gases. Furthermore, Au embedment into the WO$_3$ nanowire structures remarkably improved the performance of the sensors. The increase in response performance of sensors and adsorption–desorption kinetic processes on the sensing layers were discussed in relation with the role of Au embedment.

Gas sensors based on semiconducting metal oxides have been reported as indispensable devices that can be used in different daily applications. Compared with many other oxide materials, gas sensors based on tungsten oxide (WO$_3$), which is an n-type semiconductor because of oxygen vacancies[1], have attracted much attention because of the inherent electrical resistivity, excellent response, and selectivity of WO$_3$ to various gases. Sensing performance, particularly the response of a sensor, can be controlled by modifying the properties of sensing layer, including grain size, porosity, thickness, morphology, and impurities, by surface modification with novel metals[2]. Surface modification with catalytic novel metals particularly showed important advantages. Reactivity of a material surface and solid–gas interactions can be controlled by using various modifiers at different concentrations. For example, the configuration of d electrons of transition metals on the surface of a material can change the surface activity of the oxide semiconductor[3–5].

Metal nanoparticle decoration and doping of WO$_3$ nanostructures have been widely studied, and the modified materials showed desirable properties, thereby improving the performance of devices. Dopants modify the electronic structure by forming impurity levels in bandgaps; dopants are employed to enhance the responses of a sensor to specific gases[6–9]. In addition, decoration of metal nanoparticles on WO$_3$ surface may lead to the formation of rectifying Schottky junctions at the interfaces to alter electrical transport behavior of WO$_3$ and/or activate gas molecules that react with WO$_3$ surface. For example, Pt and Pd nanoparticles enhance the dissociation of H$_2$ molecules on WO$_3$ surface via the known spillover effect, thereby improving the performance of H$_2$ gas sensor and gaschromic devices[10,11].

In this study, we report a facile method to embed gold catalyst on highly porous WO$_3$ nanowires. The high-porosity nanowire structures of Au-embedded WO$_3$were synthesized by using porous single-wall carbon nanotubes (SWCNTs) as template, followed by tungsten deposition, dip coating in gold salt solution, and oxidation. We examined the effects of Au-embedment on structural, electrical, and gas sensing properties of the fabricated sensor. Sensors based on nanowire structures of WO$_3$ showed a significant

[1]Department of Materials Science and Engineering, Chungnam National University, Daejeon, 305-764 Republic of Korea. [2]Department of Physics, Quy Nhon University, 170 An Duong Vuong, Quy Nhon, Binh Dinh, Vietnam. Correspondence and requests for materials should be addressed to D.K. (email: dojin@cnu.ac.kr)

improvement in sensing performance towards CH_4 and H_2S gases. In particular, WO_3-based materials for CH_4 sensors have not been reported. However, the additional embedment of Au further enhanced the sensing performance. We found that the Au-embedded WO_3 sensor showed high response to CH_4. Embedding of Au nanoparticles on WO_3 surface also showed interesting response properties toward H_2S gas. The adsorption–desorption kinetic processes on the surface of Au nanoparticles and WO_3 nanowires surface were also discussed.

Results

Structural Properties.   Porous nanowires of tungsten were obtained by sputter deposition of tungsten metal on porous SWCNTs template (Fig. 1a). The characteristic nature of the open spaces of the SWCNT template was stable during the metal sputter deposition and the following oxidation processes, as previously reported[12]. The morphology was negligibly changed after immersion in Au-containing solution (Fig. 1b and Fig. S3). As seen in Fig. 1c, WO_3 nanowire structure was formed by interconnection of WO_3 grains during the oxidation process at 700 °C in air. Gold atoms on the surface also agglomerated to Au nanoparticles during the oxidation process. The distribution of Au nanoparticles was non-continuous and scattered on the surface, as revealed by the low-magnification TEM images in Fig. 2a,b. The diameter of the gold nanoparticles ranges from 8 nm to 20 nm and the average diameter of WO_3 nanowires is ~120 nm. The HR-TEM images revealed a high crystallinity of the synthesized WO_3 nanowires and gold particles. The interplanar spacing of $d_{\{202\{220\}} = 0.262$ nm in Fig. 2c is consistent with the monoclinic phase of WO_3 [JCPDF file no. 43-1035], whereas $d_{\{111\}} = 0.236$ nm in Fig. 2d correspond to the cubic phase of Au [JCPDF file no. 04–0784]. The XRD pattern of the WO_3 and Au50-WO_3 nanowire structures (Fig.3) also confirmed the formation of monoclinic phase WO_3 structure [JCPDF file no. 43-1035] and cubic phase of Au structure [JCPDF file no. 04-0784]. The bottom images show elemental mapping for W, O, and Au of the Au-embedded WO_3 nanowire. The images were obtained by STEM–energy-dispersive X-ray (EDX) spectroscopy, which suggest that gold atoms not only form nanoparticles on the WO_3 nanowire surface, but also diffuse inside of the WO_3 crystalline lattice.

To investigate the surface composition and chemical states of the elements in the sample, XPS spectra of the nanowire structures of WO_3 and Au50-WO_3 were obtained. The spectrum in Fig. 4a indicates that the surface of the samples is composed of tungsten and oxygen elements with carbon contamination. In addition, Au distribution after annealing of Au-embedded WO_3 sample is evident. The peak at 285.7 eV is attributed to CO_2, which is commonly adsorbed on the surface of the samples[13]. The high-resolution spectra of W4f (Fig. 4b) showed peaks at 35.85 and 38.02 eV, which are assigned to W4f$_{7/2}$ and W4f$_{5/2}$, respectively. These peaks corresponded to oxidation state +6 of tungsten atoms (WO_3)[14,15]. The shift of these peaks toward lower binding energy in Au50-WO_3 can be attributed to photoelectrons emitted from the lower oxidation states of tungsten (sub-stoichiometric WO_{3-x})[14]. The Au4f core level spectrum (Fig. 4c) recorded from the Au50-WO_3 sample showed peaks at 83.6 and 87.3 eV, which were assigned to Au4f$_{7/2}$ and Au4f$_{5/2}$, respectively. These data confirmed that the Au nanoparticles are in metallic state[15]. The O1s peak in Fig. 4d showed a shift to lower binding energy with Au-embedment suggesting increased defective or incomplete W–O binding via Au addition. The O1s peak could be resolved to two Gaussian function peaks (1) and (2) having binding energies of 531 and 531.8 eV for WO_3 nanowire structure, and 530.7 and 532.2 eV for Au50-WO_3 nanowires, respectively. Peak (1) may be related to oxygen in the lattice and O^{2-} ions, and peak (2) might be due to the ions of O^{2-}, O^-, and OH^- in the oxygen-deficient regions[16]. A shift of the peak (1) to lower binding energy and a shift of the peak (2) to higher binding energy were observed with Au embedment. The shift of the major peak (1) to lower binding energy with Au embedment may be attributed to the defective WO_3 or sub-stoichiometry of WO_{3-x}, whereas the shift of peak (2) may suggest an increased binding energy of the ionosorbed oxygen via Au addition. Details of the causes for the latter observation or the stronger binding of the oxygen ions on the surface are unknown, but it is consistent with the delayed surface reaction kinetics in Au50-WO_3, which will be discussed.

DC conductivity measurements.   The current–voltage (I–V) characteristics of the fabricated nanowires devices, as fundamental properties of electronic materials, were measured with varying temperatures in argon and dry air. Prior to the I–V measurements, the devices were heated to 350 °C in the given ambient conditions to remove the effect of adsorbed water molecules on the surface of the nanowires. The I–V curves of both WO_3 and Au50-WO_3 are linear, as shown in Fig. 5a-d, indicating the formation of ohmic contacts between the nanowires and Au electrodes. The resistances of nanowires calculated from the I–V measurements for pure WO_3, Au10-WO_3, and Au50-WO_3 nanowire structures are shown in Fig. 5e. The measurements in Ar ambient condition are not affected by oxygen ionosorption effect; results revealed monotonic decrease of the resistance with increasing temperature for all sensors. This relationship indicates a dominant semiconducting behavior. Therefore, the metallic nature of Au did not alter the semiconducting resistance–temperature behavior of the WO_3 nanowires probably because of the discreteness of the distribution of Au particles on the surface (Fig. 2). Nevertheless, a finite Au-embedment effect was observed, in which the resistance decreased with increasing content of embedded Au.

The increase in conduction with Au embedment can be explained by the Au-doping effect in the WO_3 lattice. This possibility could be postulated based on the EDS data in Fig. 2, which shows a uniform distribution of Au solid through the WO_3 nanowire body. Although most of the Au atoms agglomerated
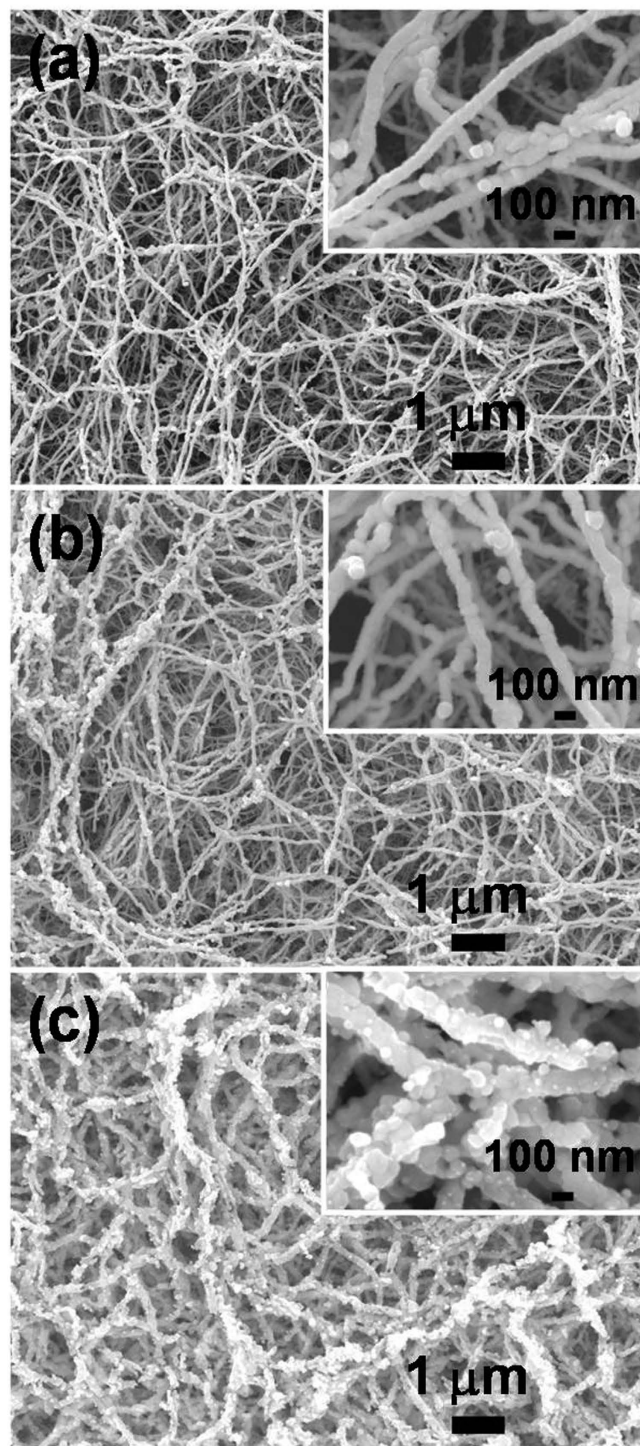
Figure 1. Morphology of the (**a**) as-synthesized tungsten-SWCNT nanowires, (**b**) tungsten-SWCNT nanowires immerged in $HAuCl_4$ solution. and (**c**) Au-embedded WO_3 nanowire structure fabricated by oxidation of (**b**) at 700 °C. Inset images show high-magnification SEM.

on the surface as nano-crystallites, some atoms are incorporated into the WO_3 nanowires during the annealing process and might form small Au clusters in the WO_3 lattice. If the conductivity of a transition metal oxide is established by hopping of electrons via dopant impurity levels, then the resistance of the oxide can be expressed by the following equation[17,18]:
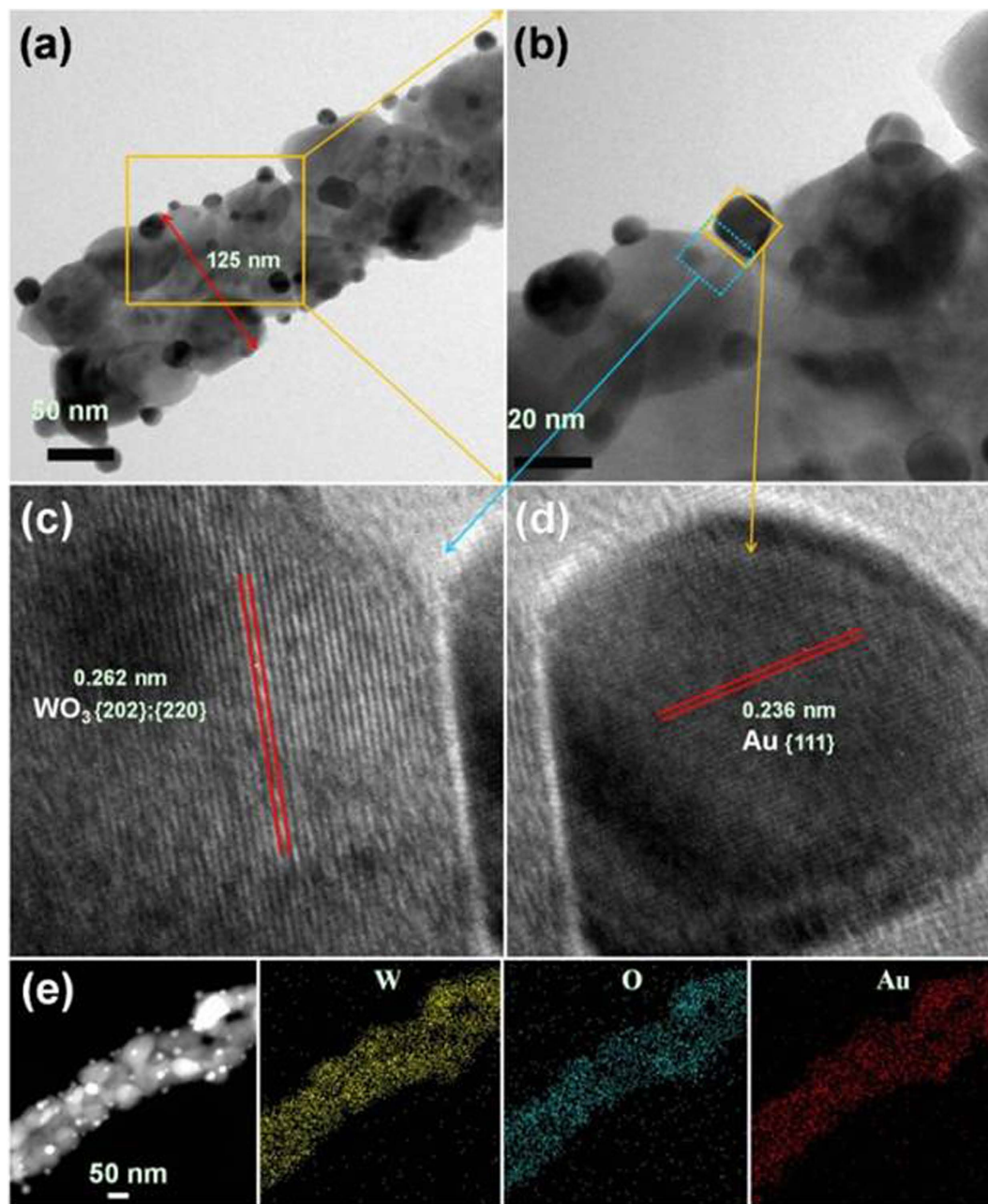
Figure 2. (**a,b**) TEM and (**c,d**) HR-TEM images of the Au-embedded WO3 nanowire structure. (**e**) STEM images and the corresponding STEM–EDX elemental mapping of the Au-embedded WO$_3$ nanowire structure.

$$R(T) = R_o \exp\left(\frac{\Delta E_a}{k_B T}\right)$$

(1)

where $R(T)$ is the resistance of a semiconductor at the absolute temperature T, ΔE_a is the thermal activation energy for hopping, and k_B is the Boltzmann constant. The temperature-dependent resistances of the pure WO$_3$ and Au-embedded WO$_3$ nanowire structures are shown in Fig. 5f, which were obtained by using the logarithm of equation (1). For pure WO$_3$ nanowires structure, we estimated the activation energies in two temperature ranges because of the slight anomaly observed at 200 °C. The activation energy values were ~0.39 eV for 200–300 °C, and ~0.29 eV for 50–150 °C. These values are all greater than the thermal activation energies of 0.27 and 0.25 eV observed for Au10-WO$_3$ and Au50-WO$_3$ nanowire structures, respectively. The decrease in activation energies with increasing Au concentration might be
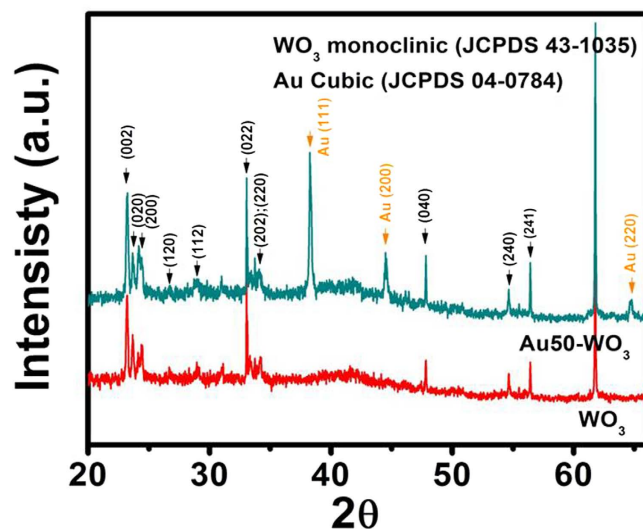
Figure 3. XRD patterns of WO$_3$ and Au-embedded WO$_3$ nanowire structures.

due to creation of additional impurities in the lattice. The distribution of Au clusters in the WO$_3$ lattice could somehow increase the oxygen vacancies. Some Au atoms may have occupied the lattice sites to play directly as a dopant. Au atoms can create impurities in the bandgap, but the observation is in agreement with the cases of In-doped CdS[19] and Al- and Sb-doped CdTe[20], which showed a decrease in activation energy with increasing dopant concentrations. In summary, the increase in conductance with Au embedment was analyzed, but a concrete conclusion cannot be elucidated at present and separate systematic study is necessary.

Interestingly, Fig. 5e shows that the temperature-dependent resistance behaviors of the Au-embedded WO$_3$ nanowires in air deviated from the semiconducting behavior at temperatures >150 °C; the resistances increased with increasing temperature. The increase in resistance is due to an enhanced oxygen ionosorption rate and corresponding increase of surface depletion depth of WO$_3$ nanowires. This phenomenon is the catalytic effect of the embedded Au nanoparticles because the pure WO$_3$ did not show such deviation even in air environment. Activation of oxygen adsorption on the surface of tin oxide decorated with various novel metals has been observed previously[21]. We found that the catalytic effect of Au critically enhances the dissociation of oxygen molecules at >150 °C, at which the adsorption ionic form of oxygen changes from O_2^- to O^-[22].

Gas sensing properties. *CH$_4$ gas sensing.* The development of resistive sensors based on metal oxide semiconductors for CH$_4$ detection has been given much research interests in recent years. Among the metal oxides, tin oxide (SnO$_2$) semiconductors have attracted particular attention[2], but sensing by WO$_3$ have been seldom reported. The CH$_4$ gas sensing properties of pure WO$_3$ and Au-embedded WO$_3$ nanowire sensors were examined and compared. The sensors exhibited a typical gas-sensing behavior of an n-type semiconductor, as shown by the decrease in sensor resistance with exposure to the reducing gas CH$_4$. The response and recovery behaviours of the Au50-WO$_3$ nanowire sensor upon exposure to 100 ppm CH$_4$ diluted in dry air was measured at different operating temperatures of 200 °C, 250 °C, and 300 °C, as shown in Fig. 6a. The response behaviours of WO$_3$, Au10-WO$_3$, and Au50-WO$_3$ sensors measured at the optimum working temperature of 250 °C are compared in Fig. 6b. The trends of temperature dependence of the sensor signal were the same in all the sensors, showing the highest response at 250 °C. The increasing Au content revealed increasing response signals, as shown in Fig. 6c. The response with pure WO$_3$ nanowire sensor was very low, which may be the reason for the limited reports on CH$_4$ gas sensing by WO$_3$-based sensor. The response enhancement was from 3% with pure WO$_3$ to 37% with Au50-WO$_3$ sensor at 100 ppm CH$_4$ and 250 °C. The sensing behaviors of Au50-WO$_3$ sensor for different CH$_4$ gas concentrations measured at 250 °C are shown in Fig. 6d. The concentration dependence of the responses for Au10-WO$_3$ and Au50-WO$_3$ are shown as the inset. Notably, the Au50-WO$_3$ sensor showed a reduced operating temperature in comparison with the SnO$_2$-based methane sensors, as shown in our previous report[23].

The enhanced response with Au embedment is ascribed to the catalytic effect of Au on the sensing process. We described the gas adsorption and desorption kinetics in relation to gas sensing of semiconducting WO$_3$ nanowires, and found that the response level and the gas selectivity of an oxide sensor is derived from the ratio of the forward (adsorption) reaction rate over the reverse (desorption) reaction rate of the relevant gas species on the oxide surface[24,25]. The higher response in the Au-embedded structure indicates that the reaction rate of CH$_4$ with ionosorbed oxygen was enhanced with respect to the recovery rate, which is determined by the oxygen adsorption rate in air. We observed that Au has a
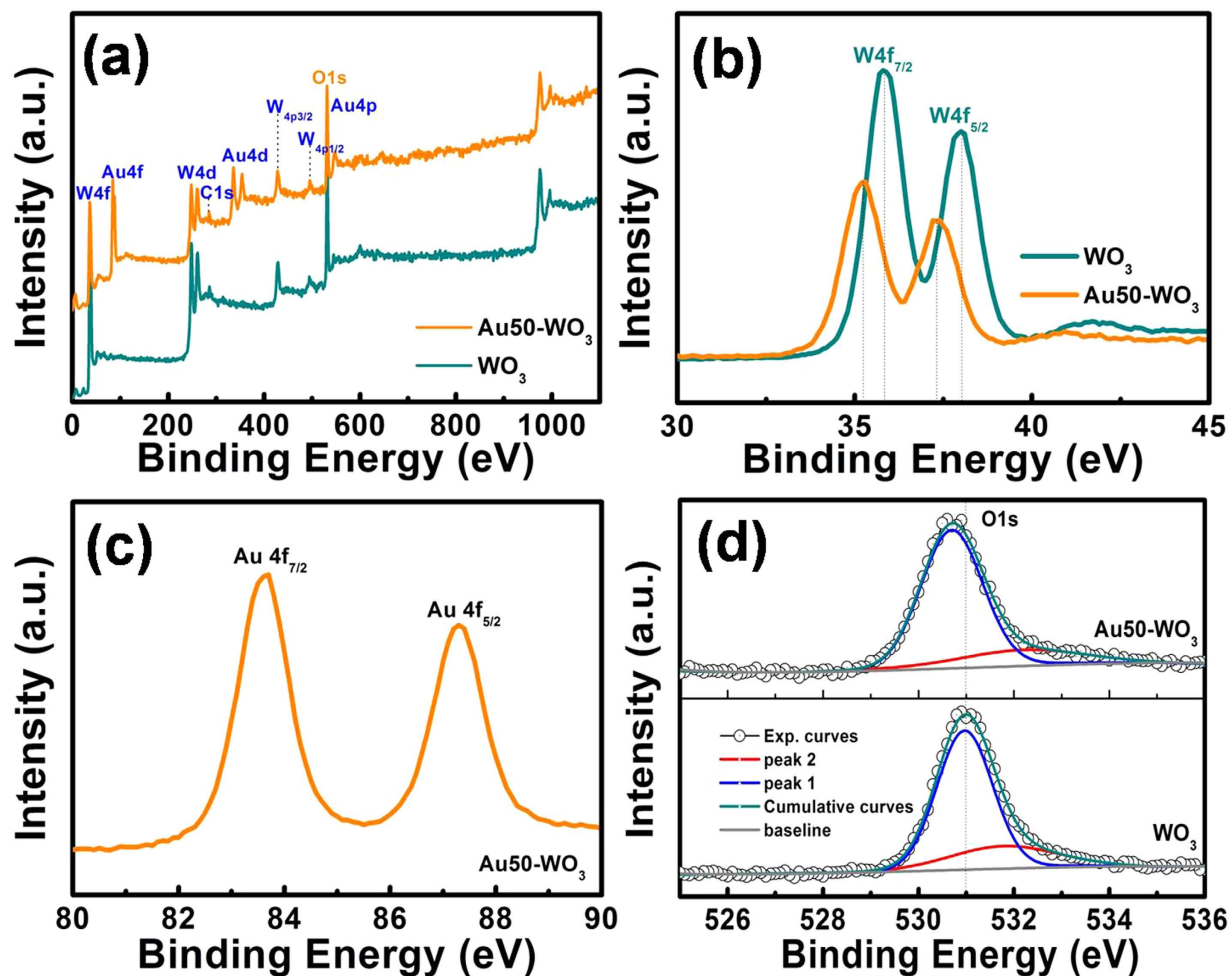
Figure 4. (**a**) XPS spectra of WO_3 and Au-embedded WO_3 nanowire structures. (**b–d**) High-resolution spectrum of W, Au, and O peaks.

catalytic effect on oxygen ionosorption and enhances the adsorption rate at >150 °C, which will enhance the recovery rate above. However, given that the enhanced response with Au-embedded sensor dictates far higher enhancement in the reaction $CH_4 + 4O^- \rightarrow CO_2 + 2H_2O + 4e^-$, gold has to further accelerate the CH_4 decomposition reaction. For example, for methane dissociated to a methyl group and a hydrogen adatom on Au surface[26], the dissociated molecular species can more actively react with the adsorbed atomic oxygen than the covalently bonded CH_4 molecules. In conclusion, Au showed catalytic effects on CH_4 dissociation and oxygen adsorption, but the rate-enhancement level was greater with CH_4 than with O_2. The net consequence was the enhanced sensor response for CH_4 with Au-embedded WO_3 sensor structures.

We also reported that a rush of reducing gas, such as H_2 and NH_3, on oxygen-ionosorbed oxide surface can produce an instant pile up of H_2O molecules on the surface, leading to an overshoot in the response cycle curves[24,25]. The similar overshoots in the response cycles were observed with CH_4 on Au50-WO_3 sensor at 250–300 °C, as shown in Fig. 6a. We believe the overshoots were also derived from the combined effect of the enhanced reaction rate at high temperature and the high impingement rate of C, H, and other fractions of CH_4 catalytically dissociated by Au.

H_2S gas sensing. The operation temperature effect of H_2S gas sensing was examined for pure WO_3 and Au50-WO_3. Fig. 7a shows the response-and-recovery curves of Au50-WO_3 nanowire sensor upon exposure to 10 ppm H_2S at different operating temperatures (171–362 °C). The response levels are summarized in Fig. 7b. Remarkable improvement in the responses by Au-embedment was observed at all the operation temperatures up to 362 °C. The sudden increase of the response times at 362 °C in both sensors was interesting (Fig. 8a). This phenomenon may be due to the catalytic decomposition of H_2S occurring in temperatures between 300 °C and 400 °C[27,28]. Thus, the species binding on the sensing layer changes at ~300 °C. Therefore, the operating temperature was set at 291 °C for the sensing of H_2S to distinguish it from the different sensing mechanisms at >300 °C.
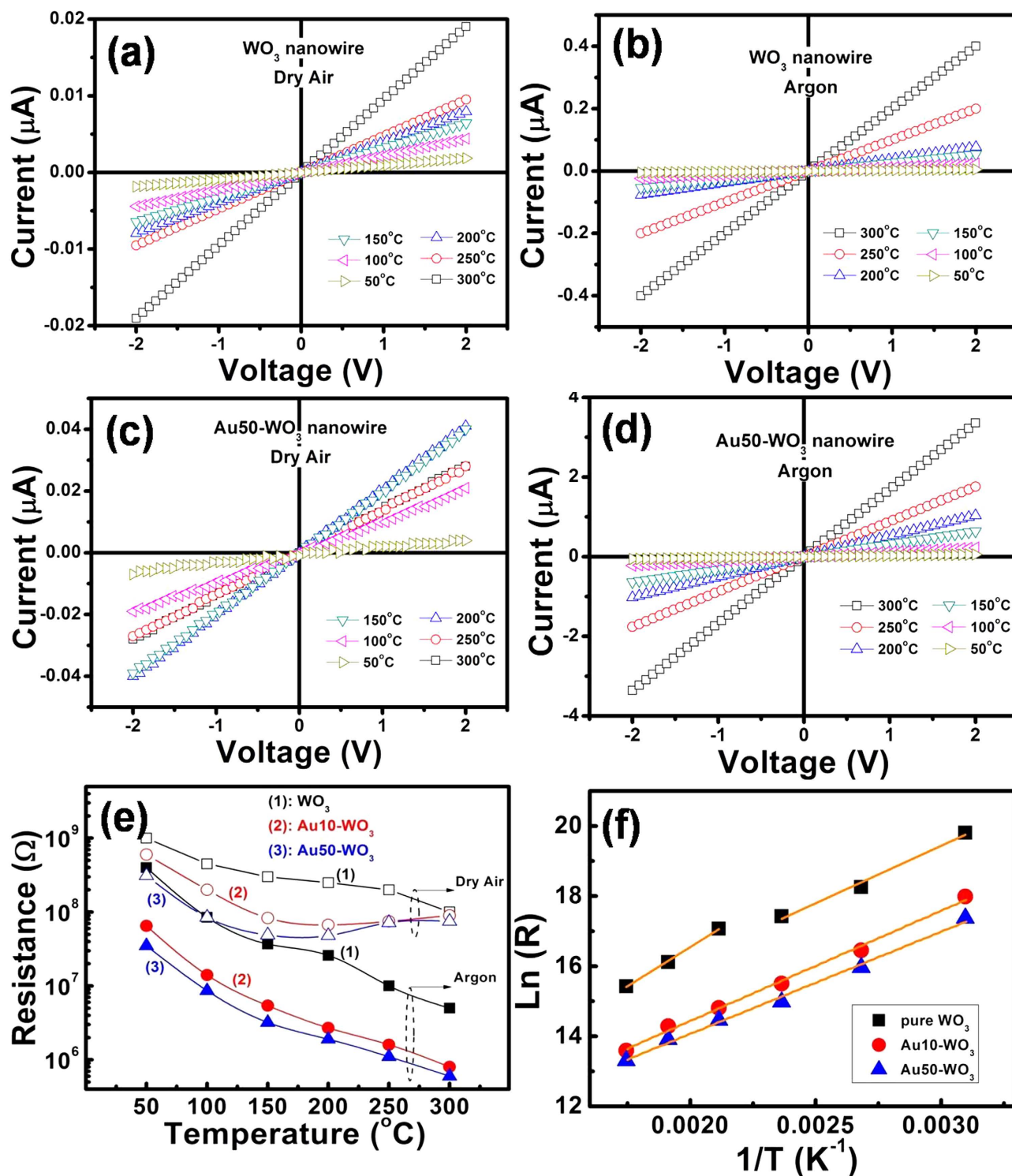
Figure 5. The current–voltage characteristics of (a,b) the WO3 nanowire sensor measured in dry air and argon ambient conditions, and (**c, d**) the Au-embedded WO3 nanowire sensor in dry air and argon ambient conditions. (**e**) Dependence of the resistance of the WO_3 and Au-embedded WO_3 nanowire sensors on different working temperatures. (**f**) The relationship between ln(R) and 1/T for the WO_3 and Au-embedded WO_3 nanowire structures in the argon condition (the straight lines show the fitting).

The response behaviors of Au_{50}-WO_3 and WO_3 nanowire sensors to H_2S were measured at various concentrations of 5, 10, 25, 50, and 100 ppm diluted in dry air at operating temperature of 291 °C, as shown in Figs. 7c, d. The responses of these sensors at different gas concentrations were also summarized in Fig. 7d, as shown in the inset. A response of 700 was obtained with the Au_{50}-WO_3 nanowire sensor
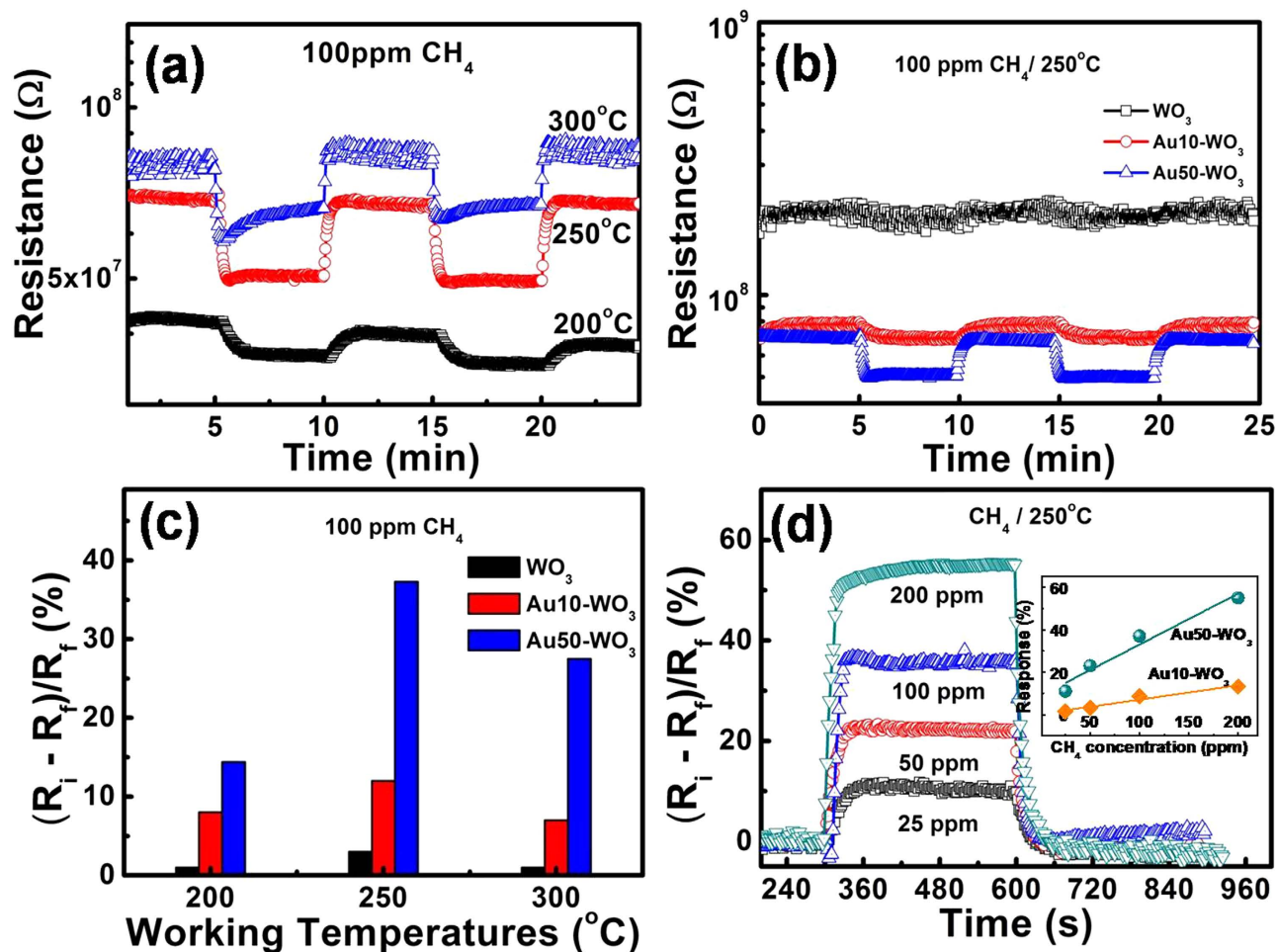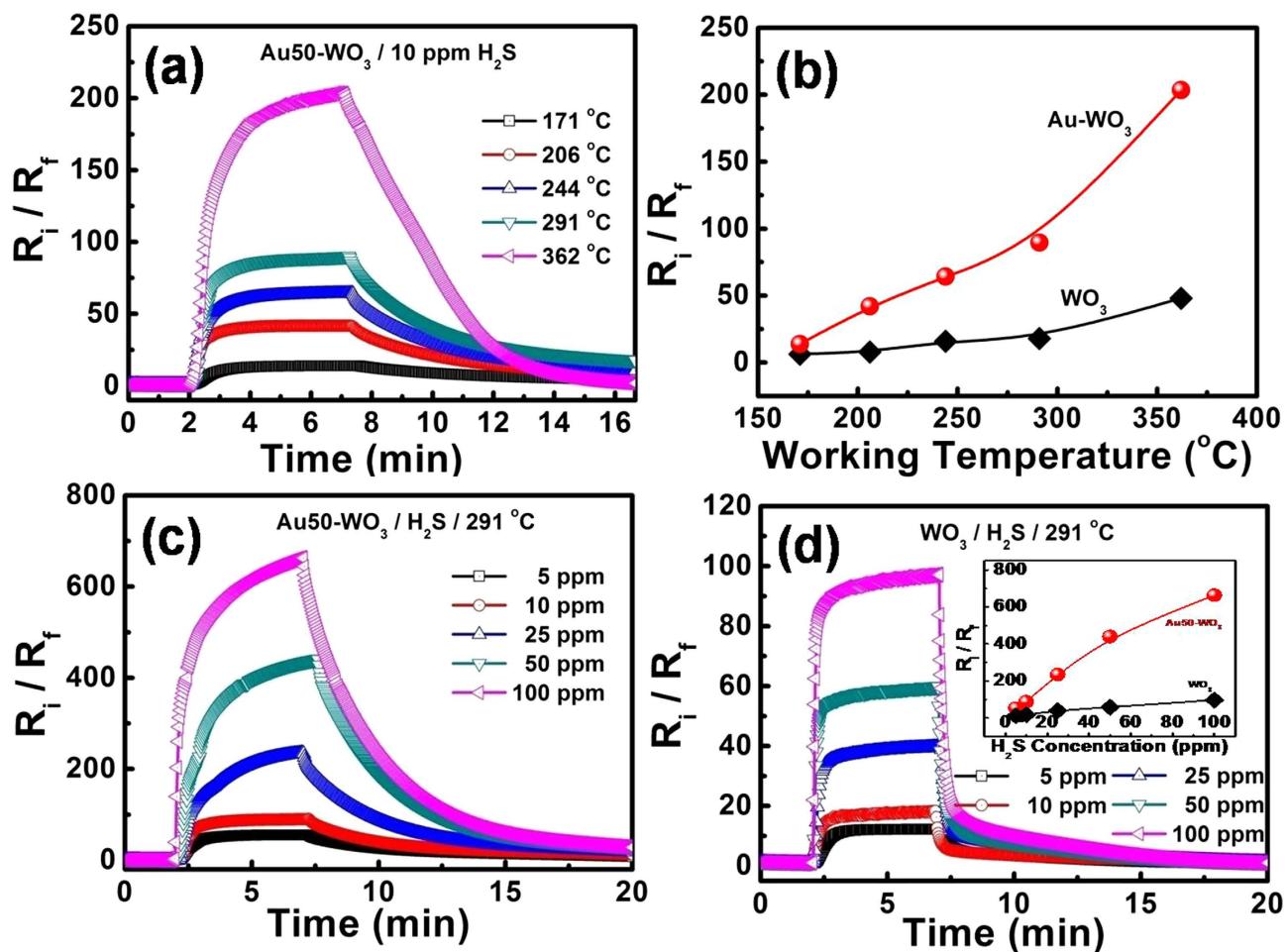
Figure 6. (**a**) Gas-sensing properties of Au50-WO$_3$ nanowire sensors upon exposure to 100 ppm CH$_4$ at different working temperatures. (**b**) Gas-sensing properties of pure WO$_3$ and Au-embedded WO$_3$ nanowire structures at optimal working temperature of 250 °C upon exposure to 100 ppm CH$_4$. (**c**) The responses of sensors to 100 ppm CH$_4$ at different working temperatures were summarized. (**d**) The response of Au50-WO$_3$ nanowire sensor to various CH$_4$ gas concentrations at optimal working temperature of 250 °C and its summary showing linearity in sensing CH$_4$ concentration (inset).

at 100 ppm H$_2$S (Fig. 7c), which is much higher than the response of 100 obtained from the pure WO$_3$ nanowire sensor (Fig. 7d). This result can definitely be explained by the catalytic effect of gold. The catalytically fractionized H$_2$S species could more actively react with ionosorbed oxygen. The WO$_3$ and Au50-WO$_3$ nanowire sensors also showed excellent selectivity to H$_2$S, as is evident from Fig. S4. The response to H$_2$S was more than two orders of magnitude higher than the response to other interfering gases, including H$_2$, NH$_3$, CO and CH$_4$ the same concentration. The selectivity towards H$_2$S was further enhanced by the Au embedding (Fig. S4).

However, the Au50-WO$_3$ nanowires showed much slower response and recovery rates compared with the pure WO$_3$ nanowires through the whole working temperatures <300 °C and the tested H$_2$S gas concentrations, as summarized in Fig. 8. Herein, the response and recovery times were measured assuming exponential rise and decay of the curves based on the first-order surface reaction kinetics for adsorption and desorption[24,25]. Therefore, they are the characteristic average times of the processes and are the times required for completion of approximately 63% (1-1/e) of the response and recovery processes. The decrease in response and recovery times with increasing working temperatures (Figs. 8a,b) is basically due to the enhanced surface chemical reaction rates in the response and recovery cycles. An exception is the abnormal increase of the response time at 362 °C with both pure WO$_3$ and Au50-WO$_3$ nanowire structures caused by the change in the formula of the species adsorbing on the Au and WO$_3$ surfaces. Its effect on WO$_3$ conductance will be discussed.

The response and recovery times measured with varying H$_2$S concentrations are shown in Figs. 8c,d. The decreasing response time with increasing gas concentrations observed with the pure WO$_3$ nanowires is the general trend in the sensing of reducing gases when the sensing behavior is based on a simple

Figure 7. (**a**) Gas-sensing properties of Au50-WO$_3$ nanowire sensors upon exposure to 10 ppm H$_2$S at different working temperatures. (**b**) Summary of (**a**) together with the measurements from WO$_3$ nanowire sensor. The response of (**c**) Au50-WO3 and (**d**) pure WO$_3$ nanowire sensors to various H$_2$S gas concentrations at optimal working temperature of 291 °C. Inset shows the summary.

chemical reaction on the surface[24,25]. However, interestingly, the response time abnormally changes with H$_2$S concentration for the Au-embedded sample, as shown in Fig. 8c. The result reveals a difference in H$_2$S gas-sensing mechanism between pure WO$_3$ and Au-embedded WO$_3$ structures.

Generally, the response levels were enhanced but the response-recovery kinetics slowed down with Au-embedment. The improved gas-sensing response levels were definitely assisted by the Au nanoparticles. As we systematically examined in Refs. 25 and 29, the response and recovery processes of the WO$_3$ sensing layer towards reducing gases are the results of thermally activated chemical reaction processes on the surface. H$_2$S gas molecules continuously react with the pre-absorbed oxygen ions (say O$^-$)[22] via

$$H_2S_{(g)} + 3O^-_{(ads)} \rightarrow H_2O_{(g)} + SO_{2(g)} + 3e^- \qquad (2)$$
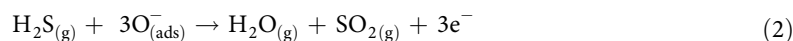
to form H$_2$O and SO$_2$. Meanwhile, oxygen molecules from the air environment continuously adsorb on the empty adsorption sites on the surface in the air atmosphere. Therefore, the response level to H$_2$S reflects the steady-state distribution of oxygen ionosorption on the WO$_3$ nanowire surface under continuous impingement of H$_2$S and O$_2$ molecules. In addition, creation of additional surface oxygen vacancies[29] due to

$$WO_3 + H_2S_{(g)} \leftrightarrow WS_2 + SO_{2(g)} + H_2O_{(g)} \qquad (3)$$
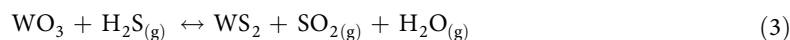
and consequent reduction of W^{6+} to W^{4+} to release electrons into the WO$_3$ nanowires was also proposed to be the reason for the response. However, a study of the detailed chemical route for sensing is beyond the scope of the present research.

Therefore, the enhanced response in Au50-WO$_3$ nanowire sensor with respect to the pure WO$_3$ (Fig. 7b) can be attributed to the highly catalytic dissociation of H$_2$S by Au nanoparticles. As can be recall
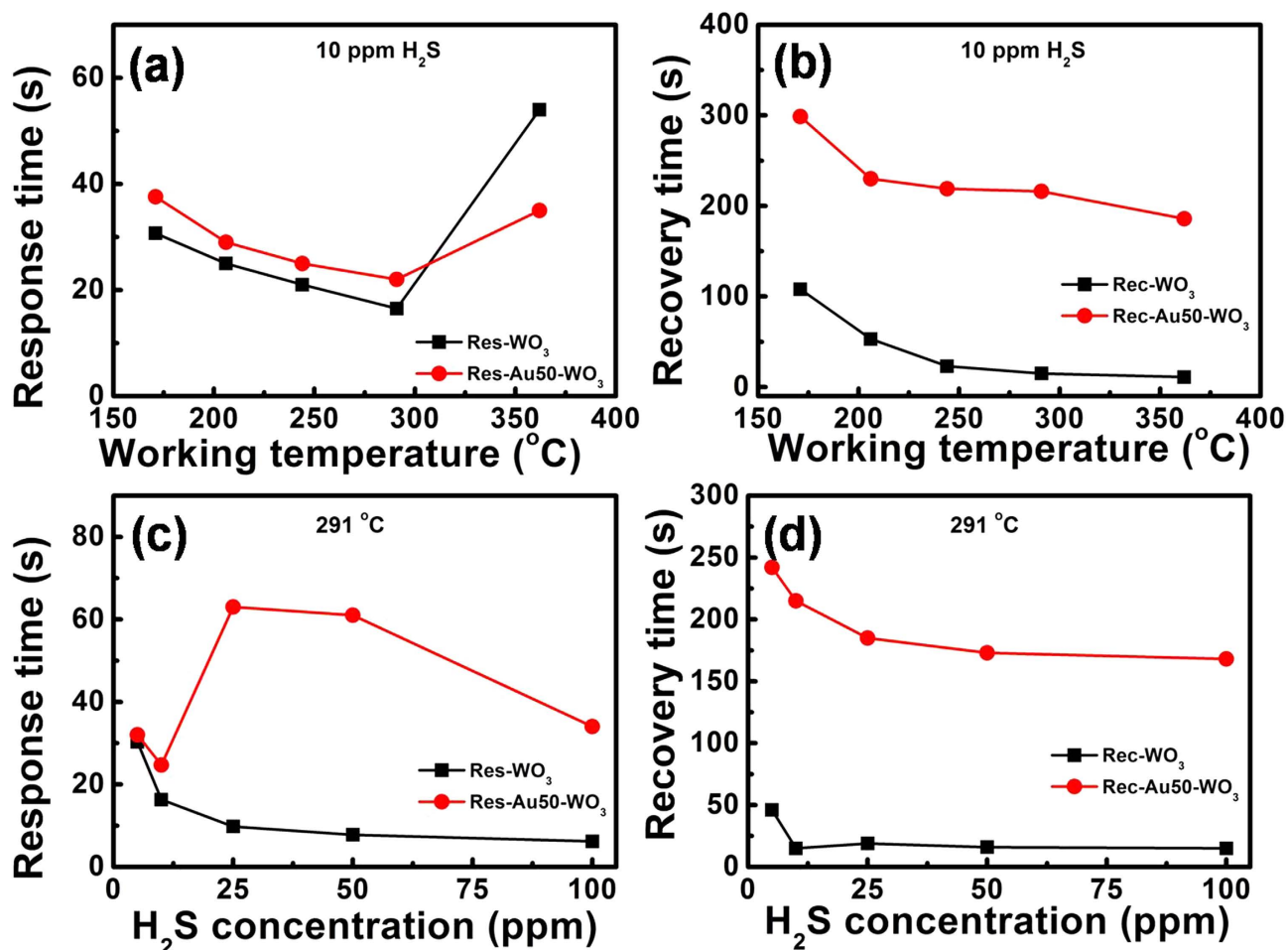
Figure 8. The response and recovery time of WO$_3$ and Au50-WO3 nanowire sensors measured (a,b) at different working temperatures to10 pm H$_2$S gas concentration, and (**c,d**) at optimal working temperatures of 291 °C on various H$_2$S gas concentrations.

from Fig. 5c, the Au nanoparticles also enhanced the dissociation rate for oxygen adsorption. Therefore, the higher response observed with Au nanoparticles than with the pure WO$_3$ could be derived from the increase in desorption rate of the adsorbed oxygen ions in equation (2), which was propelled by both of the enhanced dissociation reactions of H$_2$S and O$_2$.

A probable explanation for the enhanced catalytic role of Au in increasing the response of the sensor may be derived from the literature. H$_2$S is known to adsorb strongly onto Au because of the high chemical affinity of S on Au[30]. Leavitt and Beebe[31] found that H$_2$S decomposes to SH via

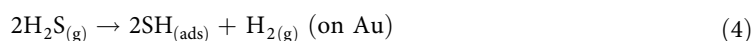$$2H_2S_{(g)} \rightarrow 2SH_{(ads)} + H_2 \qquad (4)$$

to chemisorb onto the Au surface, and the formed H$_2$ is released in the temperature range of 165–520 K. At >520 K, the adsorbed SH undergoes disproportionation to form gaseous H$_2$S and S-adsorption on the Au surface via

$$2SH_{(ads)} \rightarrow H_2S_{(g)} + S_{(ads)} \qquad (5)$$

The binding of S on Au can lower the surface work function of Au as much as 1 eV[32], so this lowering of Au work function would decrease the band bending at the interface of Au and WO$_3$ nanowires, leading to a further resistance decrease and an improved response in the Au-embedded WO$_3$ sensor. Both effects enhance the sensor response and explain the Au catalytic effect.

Now, the issues that need to be addressed are as follows: (i) the longer response and recovery times of Au-embedded WO$_3$ than WO$_3$ (Fig. 8), (ii) the abnormal increase of the response time at 362 °C (Fig. 8a), and (iii) the sudden rise of response time for higher H$_2$S concentration in Au-embedded WO$_3$ (Fig. 8c). The slower response and recovery kinetics with Au-embedment should be caused by some delayed reactions in relation to Au nanoparticles. A simple reaction of (2) may explain the sensing with

pure WO_3. The decreasing response time as the H_2S concentration increased in Fig. 8c for WO_3 reflects the concentration-dependent surface reaction rate (or $1/\tau \propto C_{H2S}$), which is observed when the surface reaction kinetics controls the sensing[24,25]. By contrast, additional reactions, such as

$$2H_2S_{(g)} \rightarrow 2SH_{(ads)} + H_{2(g)} \text{ (on Au)} \qquad (4)$$

$$H_{2(g)} + O^- \rightarrow H_2O_{(g)} + e^- \text{ (on WO3)} \qquad (6)$$

may occur with Au at relatively low temperatures. The locally generated H_2 gas molecules are added to the WO_3 surface for additional reactions. While this added surface reaction increased the sensor response level, the dissociation reaction on Au and/or the successive reaction on WO_3 surfaces delayed the overall response and recovery processes. As the H_2S concentration increased, further delayed responses were observed due to the absolute increase of the reactions, but the contribution of the reactions occurring directly on the WO_3 surface [or equation (2)] became relatively dominant at far higher H_2S concentrations, resulting in reduced response time (Fig. 8c).

For the recoveries, the simple re-adsorption of oxygen atoms on the WO_3 surface explains the recovery cycle for WO_3. However, for Au-embedded WO_3, the surfaces not only of WO_3, but also of Au particles, need to be recovered to the standby condition. In other words, chemical reactions, such as $2SH_{(ads)} + O_2 \rightarrow H_2S_{(g)} + SO_{2(g)}$ and/or $S_{(ads)} + O_2 \rightarrow SO_{2(g)}$, are required to recover to the original Au surface condition. The reactions themselves require time and may be slow, and also can influence the processes occurring on nearby WO_3 surface and finally determine the response time. For example, the produced H_2S gas from the Au surface can impinge on the WO_3 surface to play the role of analyte gas molecule and hinder the oxygen ionosorption. The delayed response and recovery rates are clear for different working temperatures and H_2S gas concentrations, as shown in Fig. 8.

Another observation is that the further slowing down of the response rate at higher temperature of 362 °C was observed in both pure WO_3 and Au-WO_3 sensor structures (Fig. 8a). Therefore, it is a temperature-related reaction kinetics that occurs on WO_3. A new reaction causing the apparently slower kinetics suddenly emerged at the above-mentioned temperature. The new reaction could be caused by the sudden change in (i) the formula of analyte gas provided and/or (ii) the ionosorbed oxygen formulas, resulting in a change in the reaction equation on the WO_3 surface. If the impinging H_2S gas molecules directly decompose to S and H_2 and adsorb on the WO_3 surface via equation (3), the high temperature further accelerates the decomposition reaction. The delayed escape of the highly increased product gas of H_2O out of the surface could increase the apparent response time. Otherwise, the direct decomposition of H_2S on the WO_3 surface via

$$H_2S_{(g)} \rightarrow S_{(ads)} + H_{2(g)} \qquad (7)$$

can be accelerated at the high temperature, thereby producing higher H_2. The increased impingement of H_2 on the surface could increase the apparent response time. The third possibility is due to the ionic form of adsorbed oxygen that may change from O^- to O^{2-} at such a high temperature $[O_2 + 4e \rightarrow 2O^{2-}_{(ads)}]$[22]. The binding energy of O^{2-} is expected to be greater than that of O^-; thus, the desorption of the former is more difficult. This situation led to the longer response time.

Conclusions

Highly porous Au-embedded WO_3 nanowire structures with diameters of ~120 nm were fabricated by tungsten deposition on porous SWCNT template, followed by dipping in $HAuCl_4$ solution and oxidation. The Au atoms coated on the W nanowire surface agglomerated to form Au crystallites on the surface and in the WO_3 lattice. The effects of Au, particularly of the embedded Au crystallites on the surface, on the gas-sensing properties were investigated based on the surface reactions. A comparison of the foregoing findings with the results obtained from pure WO_3 nanowires is useful to discuss the Au embedment effect. For CH_4 gas-sensing performance, the WO_3 nanowire structure showed a significant lowering of working temperature with respect to SnO_2 structure, whereas the Au-embedded structure demonstrated enhanced gas-sensing response because of improved dissociation of CH_4 gas molecules. A different sensing performance of Au-embedded WO_3 nanowires was observed for H_2S gas. Although the gas-sensing signals were similarly improved, the response and recovery kinetics were slowed down by Au. Such complication seems to have originated from the diverse reaction routes of H_2S gas on the Au and WO_3 surfaces. The intermediate gas products on the surface may be impinged on the surface and play the role of analyte gas (such as H_2) and/or temporarily adsorbed on the surface and show delayed detachment (such as H_2O). The Au particles embedded on the surface catalyzed the dissociation reactions of O_2, CH_4, and H_2S gases, thereby enhancing the oxygen ionosorption reaction and the gas-sensing reactions.

Methods

Fabrication of sensor structures. The Au patterned substrates were installed on the inside wall of the arc-discharge chamber; the substrate were then coated with SWCNTs, as described in Ref. 12 and 35.

Synthesis was performed at an arc current density of 40 A/cm^2 in H$_2$ gas at 400 Torr for 4 min. The carbon source used was a graphite rod that contained catalyst wires of iron, nickel, and molybdenum[12,33,34]. The SWCNT template substrates were heat-treated at 400 °C in air for 2 h to remove amorphous carbon. The SWCNT bundles seated on the substrate revealed large open spaces among the SWCNTs because of steric hindrance[12]. Tungsten metal layers were deposited on the SWCNT templates using a DC magnetron sputtering system. The deposition was performed at room temperature under a constant Ar pressure of 3.8×10^{-2} Torr and input power of 100 W for 120 s. During deposition, the substrates were rotated to attain uniform thickness. The conformal deposition of W along the porous SWCNT bundles also revealed highly porous W/SWCNT composite nanowires. Gold salt solutions were prepared by dissolving different amounts of HAuCl$_4$ salt in the mixture of distilled water and ethanol at 1:3 ratio. The W/SWCNT samples were dip-coated with Au by immersing in gold salt solutions of 0, 10, and 50 mM of HAuCl$_4$; the samples were identified as WO$_3$, Au10-WO$_3$, and Au50-WO$_3$, respectively. Oxidation of the samples at 700 °C for 2 h resulted in conversion of W to WO$_3$ and formation of Au nanoparticles while burning out the SWCNTs, leaving a highly porous tungsten oxide nanowire network. Fig.S1 shows the flowchart of the fabrication process for open-space ensemble Au-embedded WO$_3$ nanowires structure using a highly porous SWCNT template.

Characterization. Surface morphology of the nanowire structures was investigated by field emission scanning electron microscopy (FESEM; JEOL, JSM-700F) and transmission electron microscopy (TEM), scanning TEM (STEM), and high-resolution TEM (HR-TEM). The structural properties were investigated by X-ray diffraction (XRD; Rigaku D/MAX-RC) using Cu Kα radiation with a Ni filter. The electronic structure of the surface of samples was elucidated by X-ray photoelectron spectroscopy (XPS; VGMultilab 2000; Thermo VG Scientific, UK).

Gas sensing property measurement. Gas sensing properties were also measured using 6487 Keithley in a chamber with controls for temperature and gas flow[12,35]. The response of a sensor, S, was defined by R_i/R_f or $(R_i-R_f)/R_f$ for reducing gases, where R_i is the standby resistance in air, and R_f is the resistance upon exposure to reducing gas. We used 1000 ppm CH$_4$ and H$_2$S gases diluted in nitrogen as the source gas, which was further diluted in dry air at varying concentrations in the ppm range. The structure of gas sensor is shown in Figs. S2a–c. The setup for the gas sensing measurements is shown in Fig. S2d.

References

1. Gillet, M., Lemire, C., Gillet, E. & Aguir, K. The role of surface oxygen vacancies upon WO$_3$ conductivity. *Surf Sci* **532–535,** 519–525 (2003).
2. Basu, S. & Basu, P. K. Nanocrystalline Metal Oxides for Methane Sensors: Role of Noble Metals. *Journal of Sensors* **2009** (2009).
3. Drozdov, V. A. *et al.* Comparative study of the activity of Al−Pd and Al−Pt catalysts in deep oxidation of hydrocarbons. *React Kinet Catal Lett* **27,** 425–427 (1985).
4. Zhu, B. L., Xie, C. S., Zeng, D. W., Song, W. L. & Wang, A. H. Investigation of gas sensitivity of Sb-doped ZnO nanoparticles. *Mater Chem Phys* **89,** 148–153 (2005).
5. Rumyantseva, M. N., Kovalenko, V. V., Gas'kov, A. M. & Pagnier, T. Metal-oxide based nanocomposites as materials for gas sensors. *Russ J Gen Chem* **78,** 1081–1092 (2008).
6. Chen, L. & Tsang, S. C. Ag doped WO$_3$-based powder sensor for the detection of NO gas in air. *Sensor Actuat B: Chem* **89,** 68–75 (2003).
7. Zhu, S. *et al.* Synthesis of Cu-doped WO$_3$ materials with photonic structures for high performance sensors. *J Mater Chem* **20,** 9126–9132 (2010).
8. Tao, W.-H. & Tsai, C.-H. H2S sensing properties of noble metal doped WO$_3$ thin film sensor fabricated by micromachining. *Sensor Actuat B: Chem* **81,** 237–247 (2002).
9. Kawasaki, H., Ueda, T., Suda, Y. & Ohshima, T. Properties of metal doped tungsten oxide thin films for NOx gas sensors grown by PLD method combined with sputtering process. *Sensor Actuat B: Chem* **100,** 266–269 (2004).
10. Wittwer, V. *et al.* Gasochromic windows. *Sol Energ Mat Sol C* **84,** 305–314 (2004).
11. Xiang, Q. *et al.* Au Nanoparticle Modified WO$_3$ Nanorods with Their Enhanced Properties for Photocatalysis and Gas Sensing. *J Phys Chem C* **114,** 2049–2055 (2010).
12. Vuong, N. M., Jung, H., Kim, D., Kim, H. & Hong, S.-K. Realization of an open space ensemble for nanowires: a strategy for the maximum response in resistive sensors. *J Mater Chem* **22,** 6716–6725 (2012).
13. Zhang, Y.-W. *et al.* Facile Alcohothermal Synthesis, Size-Dependent Ultraviolet Absorption, and Enhanced CO Conversion Activity of Ceria Nanocrystals. *J Phys Chem B* **107,** 10159–10167 (2003).
14. Navío, C. *et al.* Gold clusters on WO$_3$ nanoneedles grown via AACVD: XPS and TEM studies. *Mater Chem Phys* **134,** 809–813 (2012).
15. Moulder, J F, Stickle, W F, Sobol, P E & Bomben, K D. Handbook of X-ray Photoelectron Spectroscopy. (Eden Prairie: Perkin Elmer) (1992).
16. Nagasawa, Y. *et al.* Photoemission study of the interaction of a reduced thin film SnO2 with oxygen. *Surf Sci* **433–435,** 226–229 (1999).
17. Mrooz, O. *et al.* Thermoelectrical degradation processes in NTC thermistors for in-rush current protection of electronic circuits. *Microelectron Reliab* **41,** 773–777 (2001).
18. Wang, X. *et al.* Gas sensors, thermistor and photodetector based on ZnS nanowires. *J Mater Chem* **22,** 6845–6850 (2012).
19. Megahid, N. M., Wakkad, M. M., Shokr, E. K. & Abass, N. M. Microstructure and electrical conductivity of In-doped CdS thin films. *Physica B* **353,** 150–163 (2004).
20. Al-Douri, A. J., Al-Shakily, F. Y., Alnajjar, A. A. & Alias, M. F. A. The Role of Dopant Concentration on Conductivity and Mobility of CdTe Thin Films. *Advances in Condensed Matter Physics* **2011** (2011).

21. Haridas, D. & Gupta, V. Enhanced response characteristics of SnO_2 thin film based sensors loaded with Pd clusters for methane detection. *Sensor Actuat B: Chem* **166–167,** 156–164 (2012).
22. Barsan, N. & Weimar, U. Conduction model of metal oxide gas sensors. *J Electroceram* **7,** 143–167 (2001).
23. Vuong, N. M. *et al.* Ni_2O_3-decorated SnO_2 particulate films for methane gas sensors. *Sensor Actuat B: Chem* **192,** 327–333 (2014).
24. Manno, D., Micocci, G., Serra, A. & Tepore, A. Thermal deposition and characterization of Se-Sn mixed oxide thin films for NO gas sensing applications. *J Appl Phys* **83,** 3541–3546 (1998).
25. Tepore, A. *et al.* Kinetic behavior analysis of porphyrin Langmuir–Blodgett films for conductive gas sensors. *J Appl Phys* **84,** 1416–1420 (1998).
26. Papadopoulos, C. A., Vlachos, D. S. & Avaritsiotis, J. N. Comparative study of various metal-oxide-based gas-sensor architectures. *Sensor Actuat B: Chem* **32,** 61–69 (1996).
27. R.B. Slimane, F.S. Lau, R.J. Dihu & Khinkis, M. Production of hydrogen by superadiabatic decomposition of hydrogen sulfide. *Proceedings of the 2002 US DOE Hydrogen Program Review*, NREL/CP-610–32405 (2002).
28. Ramgir, N. S. *et al.* Selective H2S sensing characteristics of CuO modified WO3 thin films. *Sensor Actuat B: Chem* **188,** 525–532 (2013).
29. Frühberger, B., Grunze, M. & Dwyer, D. J. Surface chemistry of H_2S-sensitive tungsten oxide films. *Sensor Actuat B: Chem* **31,** 167–174 (1996).
30. Geng, J., Thomas, M. D. R., Shephard, D. S. & Johnson, B. F. G. Suppressed electron hopping in a Au nanoparticle/H_2S system: development towards a H_2S nanosensor. *Chem Commun* 1895–1897 (2005).
31. Leavitt, A. J. & Beebe Jr, T. P. Chemical reactivity studies of hydrogen sulfide on Au(111). *Surf Sci* **314,** 23–33 (1994).
32. Mubeen, S. *et al.* Sensitive Detection of H_2S Using Gold Nanoparticle Decorated Single-Walled Carbon Nanotubes. *Anal Chem* **82,** 250–257 (2009).
33. Hoa, N. D., Van Quy, N., Cho, Y. & Kim, D. Porous single-wall carbon nanotube films formed by *in Situ* arc-discharge deposition for gas sensors application. *Sensor Actuat B: Chem* **135,** 656–663 (2009).
34. Vuong, N. M., Hieu, H. N. & Kim, D. An edge-contacted pn-heterojunction of a p-SWCNT/n-WO_3 thin film. *J Mater Chem C* **1,** 5153–5160 (2013).
35. Hoa, N. D., Van Quy, N. & Kim, D. Nanowire structured SnO_x–SWNT composites: High performance sensor for NO_x detection. *Sensor Actuat B: Chem* **142,** 253–259 (2009).

Acknowledgements

Author Contributions
N.M.V. conducted all experimental work. N.M.V. and D.K. wrote the main manuscript text. H.K. involved in discusion of XPS, gas sensing data, etc. All authors reviewed the manuscript.

Additional Information
Supplementary information accompanies this paper at http://www.nature.com/srep

Competing financial interests: The authors declare no competing financial interests.

How to cite this article: Minh Vuong, N. *et al.* Porous Au-embedded WO_3 Nanowire Structure for Efficient Detection of CH_4 and H_2S. *Sci. Rep.* **5,** 11040; doi: 10.1038/srep11040 (2015).